GEOPHYSICS, VOL. 78, NO. 5 (SEPTEMBER-OCTOBER 2013); P. D393–D402, 10 FIGS.
10.1190/GEO2013-0051.1

Mechanical properties of shale-gas reservoir rocks — Part 2: Ductile creep, brittle strength, and their relation to the elastic modulus

Hiroki Sone[1] and Mark D. Zoback[2]

ABSTRACT

We studied the elastic moduli, ductile creep behavior, and brittle strength of shale-gas reservoir rocks from Barnett, Haynesville, Eagle Ford, and Fort St. John shale in a series of triaxial laboratory experiments. We found a strong correlation between the shale compositions, in particular, the volume of clay plus kerogen and intact rock strength, frictional strength, and viscoplastic creep. Viscoplastic creep strain was approximately linear with the applied differential stress. The reduction in sample volume during creep suggested that the creep was accommodated by slight pore compaction. In a manner similar to instantaneous strain, there was more viscoplastic creep in samples deformed perpendicular to the bedding than parallel to the bedding. The tendency to creep also correlated well with the static Young's modulus. We explained this apparent correlation between creep behavior and elastic modulus by appealing to the stress partitioning that occurs between the soft components of the shales (clay and kerogen) and the stiff components (quartz, feldspar, pyrite, and carbonates). Through a simple 1D analysis, we found that a unique relation between the creep compliance and elastic modulus, independent of composition and orientation, can be established by considering the individual creep behavior of the soft and stiff components that arises from the stress partitioning within the rock. This appears to provide a mechanical explanation for why long-term ductile deformational properties can appear to correlate with short-term elastic properties in shale-gas reservoir rocks.

INTRODUCTION

We report here laboratory studies of the deformational properties of various shale-gas reservoir rocks through a suite of comprehensive laboratory experiments. Our objective was to investigate several fundamental properties of shale that may be relevant to shale-gas production. First, we report observations of time-dependent creep deformation of these rocks at differential stress conditions comparable with those in the reservoirs. Intact and frictional strengths were also reported to understand how brittle strength depends on shale composition. Although the many published empirical relations between rock strength and elastic properties imply that it is not easy to accurately predict deformational properties from petrophysical parameters (see the review by Chang et al., 2006), we also investigate the degree to which the deformational properties presented here (for example, rock strength and creep) compare with elastic properties (such as the Young's modulus) reported in our companion paper (Sone and Zoback, 2013). The relation between elastic stiffness and creep compliance is discussed quantitatively by appealing to the stress partitioning that occurs between the rock constituents using a relatively simple 1D analysis. A more accurate 3D model was also performed, which yielded similar results (Sone, 2012). Finally, some discussion on the possible relation between elastic modulus and rock strength is provided.

LABORATORY PROCEDURE

Laboratory experiments discussed here are the same experiments as those discussed in Sone and Zoback (2013). The samples come from Barnett, Haynesville, Eagle Ford, and Fort St. John shales. Mineralogy of the samples constrained by powder X-ray diffraction analysis shows that clay, quartz + feldspar + pyrite (QFP), and carbonate contents vary between 5 vol.%–50 vol.%, 5 vol.%–60 vol.%, and 0 vol.%–80 vol.%, respectively, representing a wide range of

Manuscript received by the Editor 12 February 2013; revised manuscript received 15 May 2013; published online 13 September 2013.
[1]Formerly Stanford University, Department of Geophysics, Stanford, California, USA; presently GFZ German Research Centre for Geosciences, Potsdam, Germany. E-mail: sone@gfz-potsdam.de.
[2]Stanford University, Department of Geophysics, Stanford, California, USA. E-mail: zoback@stanford.edu.

mineralogy (Figure 1). Samples from Barnett, Haynesville, and Eagle Ford shale are further divided into two subgroups with distinct mineralogy in which subgroup-1 contains more clay and organic contents than subgroup-2. Total organic contents range from 0.4 wt.%–5.8 wt.%, and porosities estimated from the mineral and bulk density range between 1.5%–9%. As described in the companion paper (Sone and Zoback, 2013), clay and kerogen content roughly correlate with each other. The porosity estimated based on the bulk and average mineral densities increases with the increase of clay and kerogen content, possibly because pore volumes in these shales mostly reside within the clay aggregates and solid organics in the sample (Loucks et al., 2009; Sondergeld et al., 2010). Microstructural observations from the companion paper (Sone and Zoback, 2013) also showed that these shales exhibit various degrees of fabric anisotropy, which is reflected on the anisotropy of their elastic properties.

Cylindrical samples of 1-inch diameter and 1.2–2.1-inch length from each sample groups were prepared with the axes either perpendicular (vertical) or parallel (horizontal) to the bedding planes. These samples were pressurized in a servocontrolled triaxial deformation apparatus to observe its static and dynamic elastic properties and creep behavior. Hydrostatic confining pressure P_c was first applied in one to four steps (hydrostatic stage), and then axial differential stress P_{diff} was applied in two to five steps while P_c was held constant (triaxial stage). The duration of each stress step was either 30 or 60 s, after which the stress was held constant for 3 h to observe the creep response. After the triaxial stage, the samples were taken to failure by loading the samples at a constant axial strain rate of 10^{-5} s^{-1} to measure rock strengths (failure stage). After rock failure, we continued to slide the failure plane to measure the residual strengths of the rock. The constant confining pressure P_c during the triaxial and failure stages was varied between 10 and 60 MPa, so that the P_c dependence of rock strengths and creep behavior could be evaluated. The magnitude of the stress steps in the triaxial stage ΔP_{diff} varied between 3 and 45 MPa to simulate differential stress states above and below in situ levels.

During the experiments, the sample deformation in the direction parallel to the cylindrical axis was measured by a pair of linear variable differential transformer displacement transducers, and the deformation perpendicular to the sample cylindrical axis (lateral deformation) was measured by a pair of spring-mounted strain-gauge transducers attached outside of the heat-shrink Viton jacket, both measurements had a displacement resolution of about 1 μm. The axial differential load was measured by an internal load cell yielding 0.3 MPa resolution for a 1-inch-diameter sample. An example of the strain response to some stress steps during the triaxial stage is shown in Figure 2. We divide the total strain response to a stress step into two parts, elastic strain ($\varepsilon_{\text{elastic}}$) and creep strain ($\varepsilon_{\text{creep}}$). We used $\varepsilon_{\text{elastic}}$ to determine the static elastic constants, and we used $\varepsilon_{\text{creep}}$ to quantify the amount of creep strain that occurs after 3 h of constant stress. Assuming that shales are transversely isotropic with the symmetry axis (x_3-axis) perpendicular to the bedding plane, we are able to determine the vertical Young's modulus E_3 and Poisson's ratio v_{31} from the vertical samples and the horizontal Young's modulus E_1 and Poisson's ratios v_{13} and v_{12} from the horizontal samples.

The maximum axial differential stress during the triaxial stage was kept below 50% of the ultimate rock strengths to assure that creep deformation did not enter its tertiary creep stage, in which strain rate starts to accelerate and lead to unstable rock failure (Lockner, 1993). We avoided the tertiary creep stage because our focus in the triaxial stage was to observe the long-term ductile property of the samples. Also high differential stress magnitudes that lead to tertiary creep are not pervasive in the crust because the crust is generally in equilibrium with the sliding frictional strength of the crustal materials (e.g., Townend and Zoback, 2001). We also note that it is unlikely that time-dependent deformation is due to poroelastic effects because the fluid saturation of the cores were at most 40%, even including clay bound water.

TRIAXIAL CREEP: GENERAL CHARACTERISTICS

The axial and lateral creep strain responses during the triaxial stage from experiments using Haynesville-1 vertical and Barnett-1 horizontal samples are compared in Figure 3a. After application of a differential stress step, the sample shrinks in the axial direction

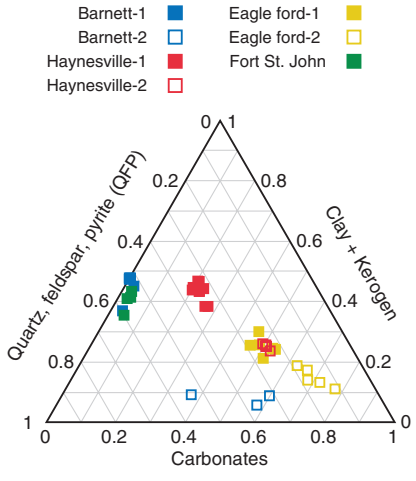

Figure 1. Ternary plot representation of the sample material compositions. Barnett, Haynesville, and Eagle Ford samples are further divided into two subgroups in which subgroup-1 samples have higher clay + kerogen content than subgroup-2 samples.

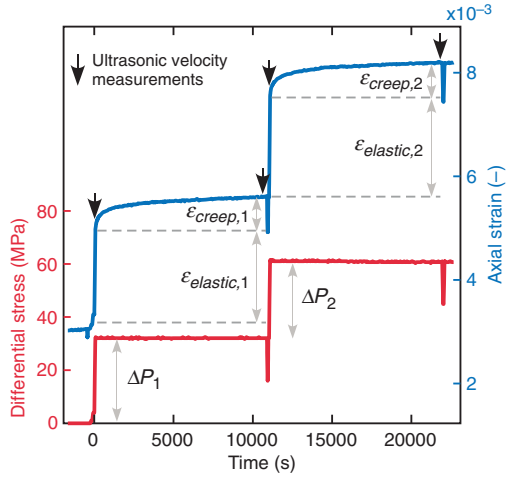

Figure 2. An example of axial differential stress and axial strain data during the stress steps in the triaxial stage. The elastic and creep strain from each stress step are used to compute the Young's modulus and the 3-h creep compliance.

and dilates in the lateral direction over time. However, although the axial strain continues to creep, lateral strain appears to stabilize after about 10 min and stay constant. The plots also show that the creep strain response is much greater in the axial direction than in the lateral direction suggesting that the sample is losing volume. Thus, most of the ductile response in these samples occurs as compaction in the direction of the applied stress.

Figure 3b displays several representative axial creep strain data observed during the triaxial stage. Even the sample that exhibited the least amount of creep (Barnett-2) shows some creep behavior, although the magnitude is very small. Note that the aluminum alloy data (Al7075, black data) tested under similar conditions showed no creep behavior. Figure 3b delineates how different the creep behavior can be between samples, but we cannot directly compare the strain responses to argue how one sample creeps more than another sample because each set of triaxial creep data was collected under different magnitudes of axial stress steps.

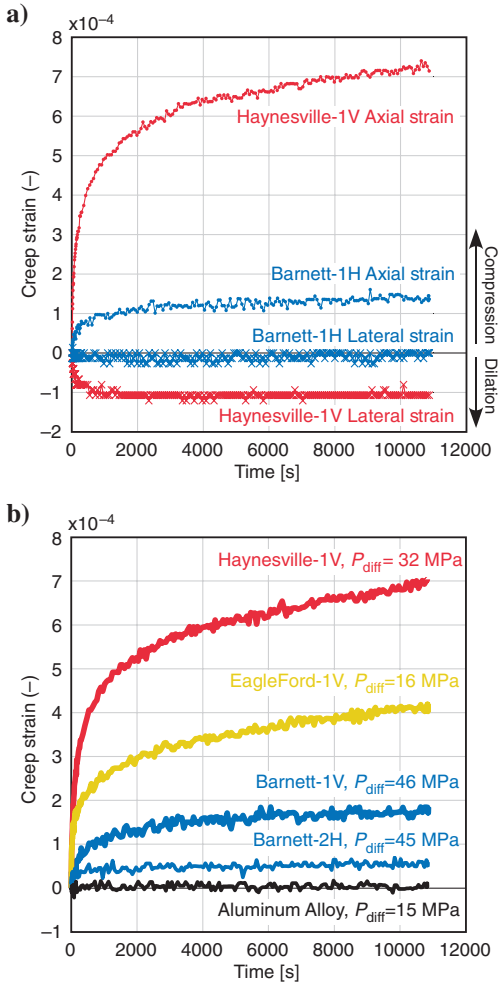

Figure 3. (a) Axial and lateral creep strain responses during the triaxial stage from a Haynesville vertical sample ($P_c = 30$ MPa, $\Delta P_{diff} = 29$ MPa) and a Barnett horizontal sample ($P_c = 20$ MPa, $\Delta P_{diff} = 48$ MPa). Note that the lateral strain stops creeping after about 1000 s. (b) Several representative axial creep strain data. A test on an aluminum alloy standard is also shown in black.

In Figure 4, the cumulative amount of creep strain, after each 3-h step is plotted against cumulative differential stress during a test. Each connected set of data points represents a single experiment with one sample. All samples show an approximately linear trend, despite the varying magnitudes of stress steps applied in each step. This suggests that the magnitude of creep strain after 3 h roughly scales linearly with the magnitude of differential stress. The slope of the linear relation represents the tendency to creep for that sample. We refer to this slope as the 3-h creep compliance S_{creep}, which is determined by linear regression and has units of MPa^{-1}. Note that the 3-h creep compliance does not describe the time-dependent constitutive relation, but it merely represents the amount of creep after a specific time of 3 h. Nonetheless, S_{creep} becomes a useful proxy for us to infer the ductility of a sample.

The 3-h creep compliance determined from our data ranges between $1e$–6 and $3e$–5 MPa^{-1}. We note that these values are significantly less than are typically observed from creep of unconsolidated reservoir rocks. Laboratory results from Hagin and Zoback (2004) using Wilmington sands show that the 6-h volumetric creep strain per megapascal of hydrostatic pressure was about $6e$–4 MPa^{-1}, and it was between $1e$–3 and $3e$–3 MPa^{-1} for weak Gulf of Mexico shales (Chang and Zoback, 2009). Thus, creep strains per unit stress change for shale-gas reservoir rocks are an order of magnitude smaller than those of uncemented sand reservoir rocks and weak Gulf of Mexico shales. We also find that the 3-h creep compliance is insensitive to the magnitude of the confining pressure during the triaxial stage. For instance, the confining pressures during the triaxial stage varied from 10 to 60 MPa in the Haynesville-1 vertical samples, but the slopes representing the creep compliances are similar to each other and do not exhibit any systematic variation with P_c (Figure 4, red circles). The same is observed from all sample groups except for the Eagle Ford vertical samples, which we suspect had greater sample variability. Therefore, the 3-h creep compliances we obtain represent the intrinsic tendency to creep for these shales that is insensitive to confining pressure and differential stress within the time scale, stress levels, and temperature condition of our experiments.

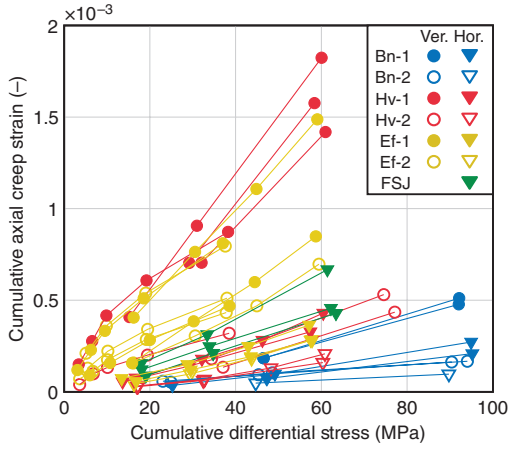

Figure 4. Cumulative creep strain versus cumulative differential stress. Each set of connected data points represents a sample, and the slope of the data points represents the approximate 3-h creep compliance: Bn, Barnett; Hv, Haynesville; Ef, Eagle Ford; FSJ, Fort St. John.

TRIAXIAL CREEP: RELATION WITH OTHER PROPERTIES

The strain data suggest that the samples compact during creep. This is also confirmed from the slight increase in dynamic moduli, measured from ultrasonic velocities, after 3 h of creep. Figure 5a shows the positive correlation between creep compliance and the percent change in P-wave modulus after 3 h of creep, which suggests that the cause of creep compaction is related to the cause of elastic stiffening. Because the applied stress and the mineral properties stay the same during creep, the overall stiffening of the samples should be the result of porosity reduction and pore stiffening, both of these being caused by pore volume compaction. Because nanostructural observations (Loucks et al., 2009; Curtis et al., 2010; Sondergeld et al., 2010) reveal that most of the pore spaces in these shale-gas reservoir rocks reside in the clays and solid organics, most of the compaction responsible for the creep deformation should be occurring within the clays and organics in the rock. This is conceivable because an increase in clay content is known to enhance creep deformation in unconsolidated shale sediments (Chang et al., 1997) and clay minerals have low friction and velocity-strengthening frictional properties that favor stable time-dependent sliding behavior unlike quartz and carbonate minerals (Moore and Lockner, 2004). Also coal, which is sometimes considered as a proxy for solid organic materials, is known to exhibit significant creep behavior from laboratory experiments (Hagin and Zoback, 2010; Yang and Zoback, 2011).

If creep deformation predominantly takes place within the clays and organics, it is naturally expected that the creep compliance of the rock increases with the amount of clays and organics in the sample. When the 3-h creep compliance is compared with the amount of total clay and kerogen volume in the rock (Figure 5b), such a positive correlation is observed when focusing on data from a single reservoir (e.g., Barnett-1 versus Barnett-2 samples). However, there does not seem to be a unique trend that explains all the data. Eagle Ford vertical samples particularly have high creep compliances despite their relatively low clay and kerogen content. This suggests that clay and kerogen content is not the only control on the creep compliance. In fact, the creep compliance is fairly anisotropic just like their elastic properties (see Sone and Zoback, 2013) such that the rock creeps more in the direction perpendicular to the bedding than in the direction parallel to the bedding. Thus, the bedding plane orientation with respect to the applied uniaxial differential stress also has a significant control on the behavior.

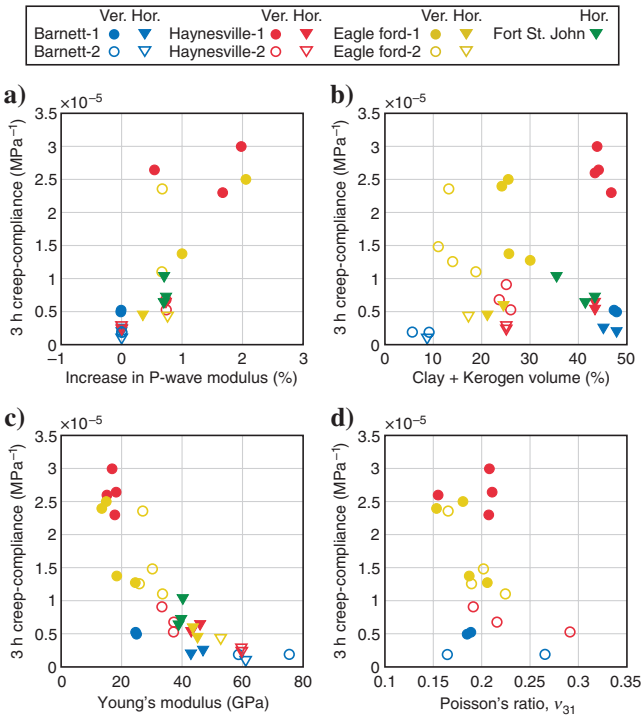

Figure 5. Three-hour creep compliance plotted against other properties. (a) Plotted versus increase in P-wave modulus after 3-h of creep. (b) Plotted versus clay + kerogen volume. (c) Plotted versus Young's modulus. (d) Plotted versus vertical Poisson's ratio.

Figure 5c and 5d shows the 3-h creep-compliance data plotted against some static elastic properties. The static elastic constants used here are those determined from the elastic strain (Figure 2) measured during the stress step. Because multiple stress steps were applied during the triaxial stage, this resulted in several measurements of static elastic constants from each sample. We use the elastic constants derived from the stress step when the axial stress (confining pressure + differential stress) was closest to 50 MPa, because 50 MPa was when most of the pressure dependence of the elastic constants became insignificant due to the closure of cracks (see Sone and Zoback, 2013). Figure 5c shows that there is a well-defined correlation between the creep compliance and the Young's modulus regardless of the clay and kerogen content or the orientation of the samples. The elastic moduli of these rocks are also dependent on material composition and orientation, thus evoking a fundamental similarity in the cause of variation in elastic properties and creep compliances. On the other hand, all types of Poisson's ratios (v_{31}, v_{13}, v_{12}) do not show any visible correlation with creep compliance.

INTACT AND FRICTIONAL ROCK STRENGTHS

As the samples were eventually taken to failure by loading in the axial direction, and all samples exhibited typical brittle behavior characterized by the rapid breakdown of rock strength from the ultimate- to residual-strength and the formation of a localized failure plane cutting through the cylindrical sample.

The ultimate strength of the intact samples (maximum axial stress upon failure) is plotted against confining pressure in Figure 6a. Assuming a Mohr-Coulomb failure criterion, a linear regression to the strength data from each sample group gives an estimate of the uniaxial compressive strength (inferred UCS) from the y-intercept and the internal coefficient of friction (μ_i) from the slope, n. The internal friction is calculated from the slope n using the following equation:

$$\mu_i = \frac{n-1}{2\sqrt{n}}. \quad (1)$$

Note that we do not distinguish between vertical and horizontal samples here because it is generally regarded that the intact rock strengths parallel to and perpendicular to the bedding plane are the same when anisotropic rock strength are interpreted to be caused by a single plane of weakness, in this case, the bedding plane being the plane of weakness (Donath, 1961; Paterson and Wong, 2005). However, the horizontal strength data tend to plot above the general trend determined by the linear regression (Figure 6a). Thus, the

intact rock strengths in our samples appear to be slightly stronger in the direction parallel to the bedding plane.

Figure 6b shows the residual strength data collected in the failure stage. The angle between the failure plane and the sample cylinder axis was measured after the experiment, and this angle was used to calculate the normal and shear tractions resolved on the failure plane during sliding. We again assume a Mohr-Coulomb failure criterion, and we obtain the sliding coefficient of friction μ_s and cohesion from the slope and y, respectively, determined through linear regression. Frictional sliding surfaces generally do not carry significant amounts of cohesion, but we consistently see about 5–15 MPa of cohesion (Figure 6b). We interpret this apparent cohesion as the sliding resistance due to the rough failure plane created by the experiment. Sliding along the failure plane reached at most about 2.5 mm in our experiments, and this was not enough to smooth out the failure plane. For the residual strength data, we do not see any dependence on the orientation of the sample.

Figure 7a and 7b compares the inferred UCS with the average total clay-kerogen volume and the average static Young's modulus of each sample group. We find that inferred UCS generally decreases with increasing clay-kerogen volume, and it has a positive correlation with the Young's modulus. As the error bars indicate, some of these values were poorly constrained, especially those from Eagle Ford-2. The uncertainty may be the result of sample variability within the sample group as the creep compliances for these samples also varied. The same trend is found when the internal

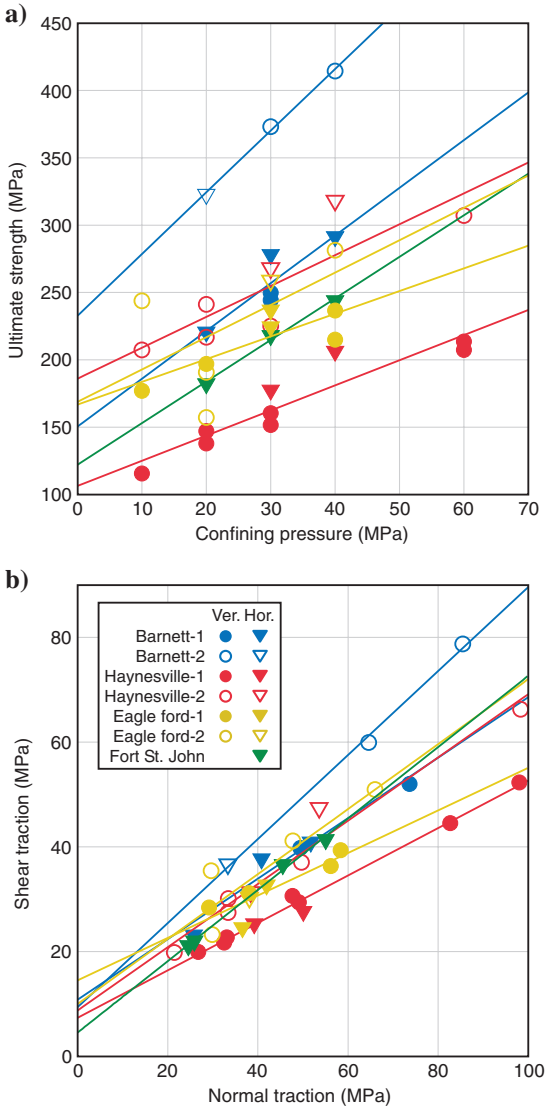

Figure 6. (a) Intact rock strength data. Axial stress upon failure (ultimate strength) plotted against confining pressure. Data from each sample group are fitted by a line to recover Mohr-Coulomb strength parameters. (b) Frictional strength data. Shear and normal traction resolved on the failure plane are plotted against each other. Again, data from each sample group a fitted by a line to recover Mohr-Coulomb friction parameters. Legends in (b) apply to (a).

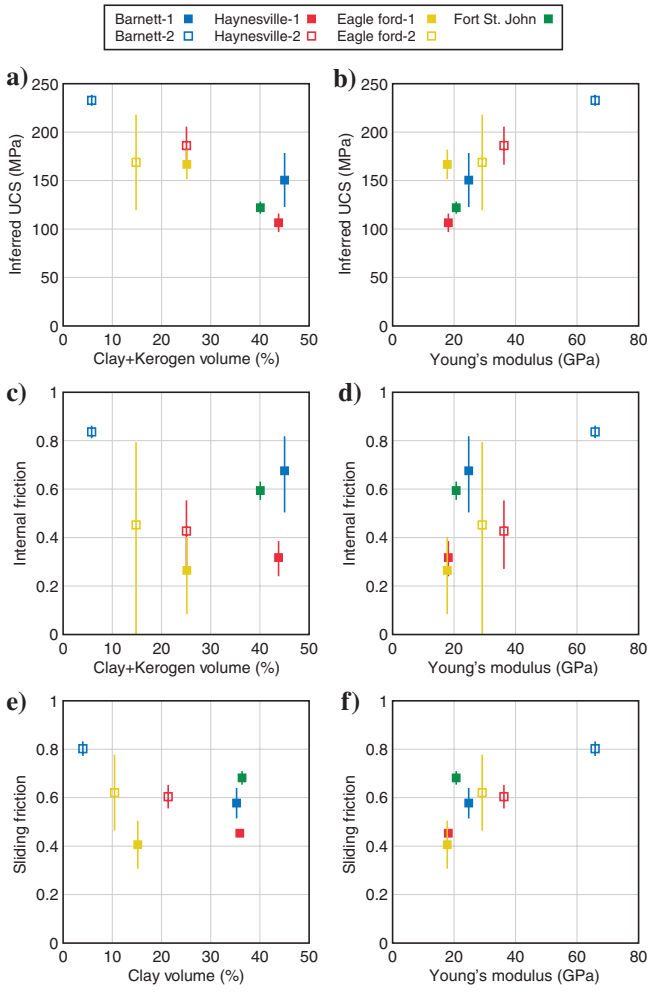

Figure 7. Strength data against composition and vertical Young's modulus. All data are average values within the corresponding groups. (a) Inferred UCS versus clay + kerogen volume. (b) Inferred UCS versus vertical Young's modulus. (c) Internal friction versus clay + kerogen volume. (d) Internal friction versus vertical Young's modulus. (e) Sliding friction versus clay + kerogen volume. (f) Sliding friction versus vertical Young's modulus. Vertical Young's modulus for Fort St. John samples was estimated from the horizontal Young's modulus using the empirical relation defined in Sone and Zoback (2013). UCS values are obtained from the linear regression shown in Figure 6a. Vertical error bars correspond to one standard deviation of the values determined from the regressions.

coefficient of friction μ_i is compared with composition and modulus (Figure 7c and 7d), although the error is somewhat greater in the determination of μ_i. Therefore, in general, the stiffer rocks have greater intact strength in these rocks, as expected.

Figure 7e and 7f compares the sliding coefficient of friction μ_s with the average clay volume and the average static Young's modulus. We compared μ_s against the clay volume, instead of the total clay and kerogen volume, because it is well known in the literature that sliding friction depends on the gouge composition (Tembe et al., 2010) and clay minerals exhibit anomalously low frictional coefficients (Moore and Lockner, 2004). However, the correlation of μ_s with the clay volume is not as robust as expected. The friction of the Eagle Ford samples is specifically low despite their low clay content. Note that there is not a significant variation in clay mineral composition because all samples mainly contained illite. Rather, we see that μ_s correlates with the elastic modulus fairly well.

RELATION BETWEEN ELASTIC AND DEFORMATIONAL PROPERTIES

Despite the fundamental differences in time scale between elastic and creep deformation, or differences in strain magnitude between elastic deformation and rock failure, the elastic modulus seems to be a fairly good indicator of rock creep compliance and strength, more so than the material composition of the rock. Although the simple notion that (elastically) compliant rocks are weaker and creeps more may be intuitive, an explanation is not readily provided. Here, we demonstrate that some correlation between the elastic modulus and deformational properties holds because both reflect the effect stress partitioning caused by the combined effect of rock composition and fabric anisotropy.

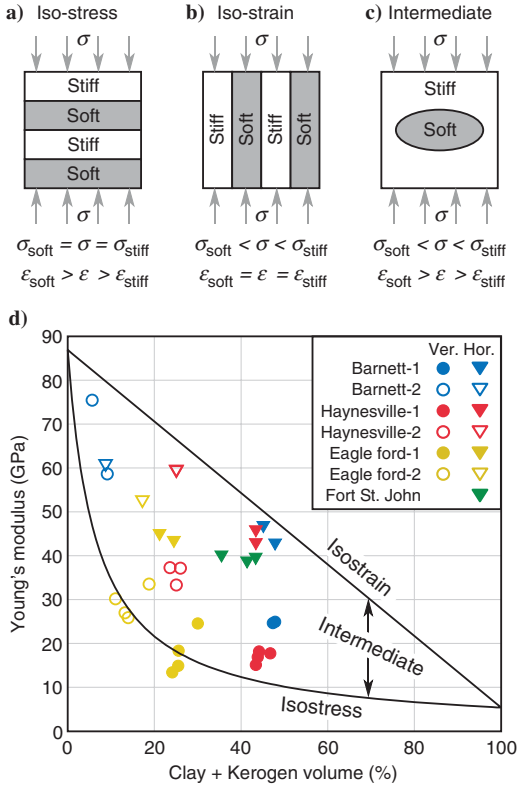

Figure 8. (a) Schematic of a layered shale model loaded perpendicular to the bedding, representing the isostress condition. (b) Schematic of a layered shale models loaded parallel to the bedding, representing the isostrain condition. (c) One example of shale models that could result in an intermediate state between isostress and isostrain conditions. (d) Laboratory Young's modulus data plotted against the sum of clay and kerogen volume, together with the Voigt and Reuss bounds calculated assuming $E_{soft} = 5.4$ GPa, $E_{stiff} = 86.9$ GPa.

CAUSE OF CREEP ANISOTROPY

We first focus on the laboratory observations that creep compliance is greater in the bedding-perpendicular direction than the bedding-parallel direction for a given type of sample. To explain this observation, we refer to a simple model in which an anisotropic gas shale rock is represented by a composite of soft and stiff layers with elastic stiffness of C_{soft} and C_{stiff}, respectively (Figure 8a and 8b). As in our companion paper (Sone and Zoback, 2013), soft layers represent clay and kerogen contents, and stiff layers represent other minerals such as quartz, feldspars, and carbonates. We then examine the stresses carried by each layer, σ_{soft} and σ_{stiff}, when a far-field uniaxial stress σ is applied to the rock. Here, we simplify the problem to one-dimension, treating stress, strain, and stiffness as scalar values. Thus, the layer properties are mechanically isotropic, and shear tractions at the layer boundaries are ignored.

When the far-field stress is loaded perpendicularly to the layers (Figure 8a), representing a vertical sample in the lab, this is an *isostress* condition in which the stresses carried by each layer are identical to the far-field stress. Thus,

$$\sigma = \sigma_{soft} = \sigma_{stiff}. \tag{2}$$

In this case, the average stiffness of the whole rock is the Reuss (harmonic) average of the stiffness of each layer. On the other hand, when the loading direction is parallel to the layers (Figure 8b), this is an *isostrain* condition and the stresses carried by each layer will be different from the far-field stress as follows:

$$\varepsilon = \varepsilon_{soft} = \varepsilon_{stiff}, \quad \frac{\sigma}{C} = \frac{\sigma_{soft}}{C_{soft}} = \frac{\sigma_{stiff}}{C_{stiff}}, \quad \therefore \sigma_{soft} < \sigma < \sigma_{stiff}, \tag{3}$$

where C is the average stiffness of the whole rock and equal to the Voigt (arithmetic) average of each layer stiffness. If creep predominantly occurs in the soft layer and the amount of creep per time is proportional to the magnitude of stress, we would expect less creep in this setting representing a horizontal sample because σ_{soft} is smaller in equation 3 than in equation 2. Because the Voigt average is greater than the Reuss average, we recover the laboratory observation that horizontal samples are elastically stiffer and have lower creep compliances.

We see from this simplified shale model that orientation affects the overall creep compliance of an anisotropic rock because it determines how the far-field stress partitions within a sample. This stress partitioning determines the stress acting on the individual components and thus the magnitude of creep in each component, and ultimately the overall creep behavior of the whole rock. The average elastic moduli of the whole rock is also affected by this stress partitioning (and strain partitioning), hence the negative correlation between elastic stiffness and creep compliance.

However, these scenarios only represent the extreme cases in which the elastic moduli lie on the Voigt and Reuss theoretical bounds (or more strictly, the bounds calculated by the Backus average (Backus, 1962) if tractions between the boundaries are considered). In reality, the elastic moduli of the gas shale samples scatter widely between the two theoretical bounds (Figure 8d) as found in Sone and Zoback (2013). This means that the stress and strain conditions in the shale samples are neither *isostress* nor *isostrain*, but some *intermediate-state* in between. Such an intermediate state can result from almost any multidimensional heterogeneous rock fabric, for instance, when one phase is suspended within the other (Figure 8c) or when one phase forms a 3D network within the other. For further generalization and discussion, we need to quantify the stress and strain partitioning in these intermediate states.

QUANTIFYING STRESS PARTITIONING

We follow the approach by Hill (1963) and first introduce the quantity P, which relates the local stress carried by one phase to the average stress that acts on a representative volume of rock. We will refer to P as the *stress-partitioning factor*:

$$\sigma_i = P_i \sigma (i : \text{soft}, \text{stiff}). \tag{4}$$

Because stress is a tensor quantity, P_i is generally a fourth-rank tensor that depends on the volumetric fractions, spatial distribution, and elastic properties of the individual constituents and the average elastic property of the whole rock. Frequently, P_i (or the strain counterpart Q_i) is used in effective medium theory (e.g., Bayuk et al., 2007; Bandyopadhyay, 2009), and the forward determination of the exact form is a fairly involved problem of elasticity. Here, we reduce our analysis to one dimension again, treating stress as a scalar quantity, and we also treat P_i as a scalar quantity. Such simplification of the problem ignores traction between phase boundaries and the stress heterogeneity within a given phase. However, we found only small differences in the results when the following analyses were conducted numerically by 3D effective medium approaches using tensor forms of P_i for ellipsoidal inclusions (Sone, 2012). Thus, the following analyses provide a useful framework to understand our problem, but only correct to the first order.

Maintaining notations from the previous section and the idea of viewing gas shales as binary mixtures of soft and stiff components, the definition of average stress and strain give the following relations:

$$\sigma = x_{\text{soft}} \sigma_{\text{soft}} + x_{\text{stiff}} \sigma_{\text{stiff}}, \tag{5}$$

$$\varepsilon = x_{\text{soft}} \varepsilon_{\text{soft}} + x_{\text{stiff}} \varepsilon_{\text{stiff}}, \tag{6}$$

where x_i is the volumetric fraction of the components ($0 < x_i < 1$). By replacing individual stresses σ_i in equation 5 using equation 4, we obtain

$$1 = x_{\text{soft}} P_{\text{soft}} + x_{\text{stiff}} P_{\text{stiff}}. \tag{7}$$

By replacing individual strains ε_i in equation 6 with individual stress σ_i and individual stiffness C_i, and also using equations 4 and 7, we obtain an expression for the average stiffness $C (= \sigma/\varepsilon)$:

$$\frac{1}{C} = \frac{r_{\text{soft}}}{C_{\text{soft}}} + \frac{1 - r_{\text{soft}}}{C_{\text{stiff}}} \quad (r_i = x_i P_i). \tag{8}$$

This equation takes a similar form to the Reuss average of the stiffness or the Voigt average of the compliance ($= 1/C$), with the only difference being the r_i that replaces the volume fraction, x_i. The average elastic moduli in the intermediate state are thus obtained through modification of common averages (e.g., Voigt and Reuss) in which the weighting coefficients x_i are further weighted by multiplying P_i. However because determining P_i from knowledge about the rock fabric can be involved, forward calculating the average moduli using equation 8 is not always easy. Note that the reciprocity between stiffness and compliance leads to a similar set of equations for the strain-partitioning factors (i.e., Q_i) and average compliance.

Equation 8 also shows that we can solve for the stress-partitioning factor P_i if we know the average elastic property of the whole rock, given volumetric fractions, and elastic properties of the individual constituents. In other words, by knowing the constituent minerals and the outcome of mixing them, we can infer how the constituents are mixing mechanically (how stress and strain are partitioning) without detailed knowledge of the rock fabric that is causing it. By solving for P_i in equation 8, we obtain

$$P_i = \frac{1}{x_i} \cdot \frac{C_i}{C} \cdot \frac{\Delta C - |C - C_i|}{\Delta C} \quad (\Delta C = C_{\text{stiff}} - C_{\text{soft}}). \tag{9}$$

We can now use equation 9 to quantify the stresses carried by each component (soft and stiff) from the material composition and laboratory-measured average modulus for any shale samples whose moduli lie between isostrain and isostress conditions (Figure 8d).

Figure 9 shows the range of values P_i taken in the intermediate state between the two bounds for the Young's modulus shown in Figure 8d, at 0%–60% soft component volume. We calculate P_i using equation 9 based on composition, x_i, and the average Young's modulus as the average stiffness C. As suggested from equation 2, P_{soft} and P_{stiff} are equal to one along the Reuss lower bound of the Young's modulus confirming the isostress condition. Then, P_{soft} and P_{stiff} change continuously to lower and higher values, respectively, as the average stiffness increases toward the Voigt upper bound. When the average stiffness equals the Voigt upper bound, P_i is equal to C_i/C_{voigt} as determined by equation 3. Along the Voigt upper bound, $P_{\text{stiff}}/P_{\text{soft}} = C_{\text{stiff}}/C_{\text{soft}} = 16.1$; thus, the stress carried by the stiff components is 16 times higher than the stress carried by the soft components.

CREEP COMPLIANCE VERSUS YOUNG'S MODULUS

Now, we consider the forward determination of the bulk rock creep compliance using the stress-partitioning behavior obtained above. Honoring the definition of elastic strain in equation 6, we assume that the total 3-h creep strain of the rock can be described similarly as

$$\varepsilon_{\text{creep}} = x_{\text{soft}} \varepsilon_{\text{creep,soft}} + x_{\text{stiff}} \varepsilon_{\text{creep,stiff}}. \tag{10}$$

Then, if we define 3-h creep compliances for the individual components S_{soft} and S_{stiff} similar to S_{creep} defined for the whole rock,

$$\varepsilon_{creep} = x_{soft}\sigma_{soft}S_{soft} + x_{stiff}\sigma_{stiff}S_{stiff}. \quad (11)$$

Replacing individual stresses with stress-partitioning factors using equation 4, the overall 3-h creep compliance of the rock is described as

$$S_{creep} = r_{soft}S_{soft} + (1 - r_{soft})S_{stiff}. \quad (12)$$

Note that we have made an important assumption here that the elastic stress exerted on the individual components stays the same throughout the creep deformation despite the plastic strain taking place. Because creep strain taking place in our experiments is on the order of $1e-4$, and the resulting change in elastic modulus is at most 2% (Figure 5a), this is small enough to preserve the internal stress partitioning behavior within the rock after the creep.

Finally, combining equations 9 and 12 by eliminating $r_i(= x_iP_i)$, we obtain a unique relation between the 3-h creep compliance and the average elastic modulus of the whole rock:

$$S_{creep}(C) = \frac{1}{C}\cdot\frac{C_{stiff}C_{soft}}{\Delta C}(S_{soft} - S_{stiff}) + \frac{C_{stiff}S_{stiff} - C_{soft}S_{soft}}{\Delta C}. \quad (13)$$

Thus, the 3-h creep compliance (S_{creep}) is an inverse-proportional function of the elastic modulus (C), independent of the composition or the orientation of the rock. Note that this relation appears much similar to the inverse proportionality between the elastic-compliance and elastic stiffness. In fact, if we set $S_i = 1/C_i$, equation 13 becomes merely a redundant derivation of the inverse proportionality between average elastic compliance and average elastic modulus ($S_{elastic} = 1/C$). The similarity in the functional form between elastic and creep compliances arises because we defined the 3-h creep strain to be proportional to the applied differential stress in equation 11 (based on the observations shown in Figure 4), similar to elastic strain. But S_{creep} has an additional offset defined by the second term in equation 13, which only vanishes in the special case when the individual creep compliances are proportional to their elastic compliances ($C_iS_i =$ constant). Because elastic and creep deformation are caused by fundamentally different physical mechanisms, such a coincidence will not be the case as shown in the next section and the offset created by the second term distinguishes equation 13 from a simple inverse proportionality.

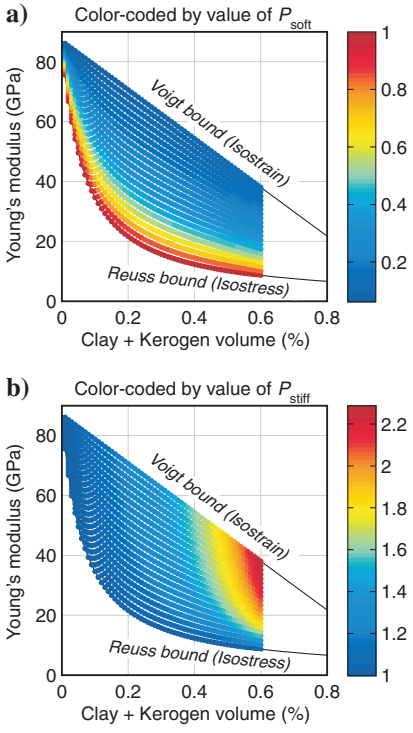

Figure 9. The Young's modulus versus soft component volume color coded by the value of the corresponding stress-partitioning factor. (a) Color coded by P_{soft}. (b) Color coded by P_{stiff}. The Voigt and Reuss bounds are the same as those shown in Figure 8d calculated assuming $E_{soft} = 5.4$ Gpa, $E_{stiff} = 86.9$ GPa.

COMPARISON WITH LABORATORY DATA

To validate equation 13 with our laboratory data, we need to define the individual elastic and creep properties of the soft and stiff components (C_i and S_i). We have thus far treated the rock stiffness as a generic scalar property C in previous sections because the algebra was simplified to one dimension, but from here on, we use the Young's modulus E as the elastic stiffness representing C. The Young's modulus is appropriate because the 3-h creep-compliance data reflect the axial creep strain caused by uniaxial loading, similar to the axial elastic strain that defines Young's modulus. We use the values $E = 86.9$ GPa and $E = 5.4$ GPa as the Young's modulus of the soft and stiffness components, respectively, because these values were found to best explain the scatter of static Young's modulus data from Sone and Zoback (2013).

There exists no direct measurement of S_{soft} and S_{stiff}, so we infer these from several laboratory data. First, we refer to the stiffest samples from Barnett-2, and we make a rather unrealistic assumption that the creep strains only take place in the stiff components ($S_{soft} = 0$) to determine the upper limit value for S_{stiff}. Using equations 9 and 12 with $E = 70$ GPa for the average Young's modulus of Barnett-2 samples,

$$\max(S_{stiff}) = \frac{S_{creep,Barnett-2}}{r_{stiff,Barnett-2}} \approx \frac{1.5*10^{-6}}{0.98} \approx 1.5*10^{-6}\ [\mathrm{MPa}^{-1}]. \quad (14)$$

Now we refer to the Eagle Ford-1 vertical samples, one of the most compliant samples whose Young's modulus lies on the Reuss bound; thus, $P_i = 1$. Because the 3-h creep compliances of these rocks are on the order of $S_{creep} = 2.5e-5$ MPa^{-1} (Figure 5a), we easily recognize that the contribution to the whole rock creep compliance from the stiff component is negligible even if S_{stiff} took its maximum possible value estimated in equation 14. Thus, we can ignore the contribution by the stiff component and estimate the value of S_{soft} as

$$S_{soft} \approx \frac{S_{creep,EagleFord-1}}{r_{soft,EagleFord-1}} \approx \frac{2.5*10^{-5}}{0.25} = 1*10^{-4}[\mathrm{MPa}^{-1}]. \quad (15)$$

Now coming back to the Barnett-2 samples with the above value $S_{soft} = 1e-4$ MPa^{-1}, we recognize by using equations 9 and 12

that the contribution of creep from the soft component matches the magnitude of the whole rock creep behavior:

$$r_{\text{soft,Barnett}-2} S_{\text{soft}} \approx 0.016 * 1 * 10^{-4}\ [\text{MPa}^{-1}] \approx 1.5 * 10^{-6}\ [\text{MPa}^{-1}]. \quad (16)$$

Therefore, the stiff component is again not contributing to the whole rock creep deformation and S_{stiff} should be at least one order smaller than determined by equation 14 or practically zero compared to S_{soft}. Although these are coarse estimates of the individual creep compliances, these values for S_{soft} and S_{stiff} confirm the idea that the majority of creep occurs in the soft components.

Figure 10 compares the laboratory data with the predicted relation between 3-h creep compliance and the Young's modulus. We find that equation 13 captures the trend of the entire data set fairly well. Note that the two thin red curves in Figure 10 are inverse-proportional relations scaled vertically to match the data with the highest elastic stiffness and the data with the highest creep compliance. Both of these curves do not fit the overall trend of the laboratory data; thus, the full functional form of equation 13 with the offset term is needed to explain the laboratory-observed trend. Therefore, the unique relation between 3-h creep compliance and the Young's modulus found in the lab is successfully explained by the derivations leading up to equation 13, which acknowledges the stress partitioning between the individual components within the shale and the contribution of creep strain by the individual components.

Finally, we note that a similar analysis in three dimensions was performed with an effective medium approach in Sone (2012). The numerical differential effective medium model was used to characterize the stress partitioning between soft ellipsoidal inclusions embedded in a stiff matrix. The resulting relation between creep compliance and the Young's modulus is not purely unique as in equation 13 due to the treatment of tractions between phases within the rock structure, but the effective medium approach yielded the same conclusions. Thus, our simplified 1D approach used in this paper seems to successfully capture the essence of the problem.

INSIGHTS ON INTACT ROCK STRENGTH ANISOTROPY

Although appealing to the stress partitioning between the components constructing the rock is successful in predicting the creep behavior, it is quite difficult to apply the same concept to discuss the apparent correlation observed between rock strength and elastic properties. The discussion from the previous section was possible because the creep deformation was small enough to preserve the elastic structure of the rock, and thus the elastic calculation of stress partitioning was valid throughout the creep process. However, rock strengths are measured at the point of rock failure, and processes leading up to rock failure do not preserve the elastic structure of the rock. As observed from acoustic emissions studies, rocks first start to fail by hosting microscale failures distributed throughout the rock specimen (Lockner et al., 1992). Then, as the number of microcrack increases, they coalesce into larger fractures that ultimately develop into a macroscopic failure plane. These microcracks are permanent damage to the elastic structure of the rock, and the process of fracture coalescence is a highly nonlinear process not captured by simple elastic models. Moreover, the dependence of strength on the confining pressure can only be discussed by introducing some frictional process. Therefore, it does not seem straightforward to argue why the apparent correlation between various rock strength parameters and Young's modulus exist as in Figure 7 and observed elsewhere in the literature (Fjaer et al., 1992; Chang et al., 2006).

However, the stress-partitioning behavior examined in the previous sections may provide some insights into why rock strengths appear to be stronger in the direction parallel to the bedding than in the direction perpendicular to the bedding as observed here (Figure 6a) and in other data in the literature (see Paterson and Wong [2005] and references therein). Because the stress-partitioning behavior is different depending on the direction of the applied uniaxial load, the timing of the onset of microfracturing could be different between vertical and horizontal samples, which may ultimately control when these microfractures coalesce into a macroscopic fracture plane. If we assume that the soft component fails locally before the stiff components, because clay-rich shales are generally weaker than quartz/carbonate rich shale, the onset of microfracturing should occur at a lower stress level when a given anisotropic shale rock is loaded perpendicular to the bedding plane. This may result in a weaker strength in the bedding-perpendicular direction compared to the bedding-parallel direction for anisotropic rocks. It is interesting to refer to the experiments using gneiss samples by Rawling et al. (2002), in which differences in microcrack development were observed between samples loaded perpendicular and parallel to the foliation. Rawling et al. (2002), together with data from Shea and Kronenberg (1993), also suggest that the abundance of the weak phase (mica in their gneiss samples) correlate with the initial damage state of the sample, which strongly influences the timing of crack coalescence and peak strength of the rock. Observation of the microscale processes leading up to rock failure in shales should help us understand the importance of fabric anisotropy on intact rock strengths of shales.

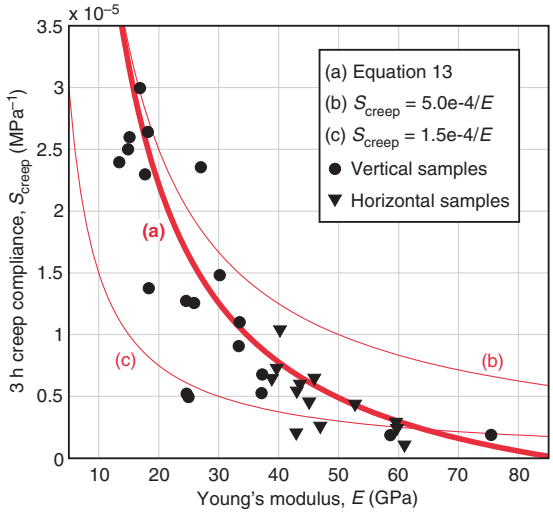

Figure 10. Comparison between predicted and observed relation between 3-h creep compliance and elastic Young's modulus. Bold red curve is drawn by equation 13 using the following constant values: $E_{\text{soft}} = 5.4$ Gpa, $E_{\text{stiff}} = 86.9$ GPa, $S_{\text{soft}} = 1e-4$ MPa^{-1}, and $S_{\text{stiff}} = 0$ MPa^{-1}. The two thin red curves are inverse-proportional relations scaled to match the data point with highest Young's modulus and highest creep compliance.

CONCLUSIONS

We have shown through laboratory experiments that the ductile creep property and brittle strengths of shale-gas reservoir rocks are dependent on material composition and sample anisotropy. Creep deformation is generally more pronounced in samples with higher clay and organic content but is also strongly affected by the direction of loading with respect to the bedding plane. Brittle rock strengths were also affected by the clay and organic content, and a slight anisotropy in intact rock strengths was also observed. However, ductile creep and brittle strengths properties exhibited the strongest correlation with the elastic modulus of the rocks, although ductile and brittle deformations are caused by fundamentally different mechanisms from elastic deformation.

We showed through a shale model consisting of a binary mixture of soft and stiff components that the apparent unique correlation between the creep compliance and elastic modulus can be explained by appealing to the stress partitioning that occurs in the rock and by reconstructing the whole rock creep behavior according the stress-partitioning information. Therefore, although creep and elastic deformation are fundamentally different processes, their quantitative relation can be established as long as the internal stresses causing those deformations are the same and those stresses can be examined quantitatively. However, the apparent relation between brittle strengths and elastic properties of the shale rock still remains a difficult observation to provide a quantitative explanation. The internal stress heterogeneity caused by the stress-partitioning effect may provide some insights, but the coalescence of microcracks into a macroscopic failure plane that takes place before rock failure cannot be captured by elastic models. Thus, further characterization of the plastic processes leading up to rock failure is needed to understand the possible relation between brittle rock strengths and elastic properties.

ACKNOWLEDGMENTS

We thank BP, ConocoPhillips, and Unconventional Gas Resources for providing us with the core samples and data necessary to carry out this research. We also thank Gary Mavko and Jack Dvorkin for the valuable discussions, and the reviewers for their constructive comments. Financial support was provided by the Stanford Rock Physics and Borehole Geophysics (SRB) Industrial Consortium, Chevron, and ConocoPhillips.

REFERENCES

Backus, G. E., 1962, Long-wave elastic anisotropy produced by horizontal layering: Journal of Geophysical Research, **67**, 4427–4440, doi: 10.1029/JZ067i011p04427.

Bandyopadhyay, K., 2009, Seismic anisotropy: Geological causes and its implications to reservoir geophysics: Ph.D. thesis, Stanford University.

Bayuk, I. O., M. Ammerman, and E. M. Chesnokov, 2007, Elastic moduli of anisotropic clay: Geophysics, **72**, no. 5, D107–D117, doi: 10.1190/1.2757624.

Chang, C., D. Moos, and M. D. Zoback, 1997, Anelasticity and dispersion in dry unconsolidated sand: International Journal of Rock Mechanics and Mining Sciences and Geomechanics Abstracts, **34**, 402, doi: 10.1016/S0148-9062(97)00094-6.

Chang, C., and M. D. Zoback, 2009, Viscous creep in room-dried unconsolidated Gulf of Mexico shale (I): Experimental results: Journal of Petroleum Science and Engineering, **69**, 239–246, doi: 10.1016/j.petrol.2009.08.018.

Chang, C., M. D. Zoback, and A. Khaksar, 2006, Empirical relations between rock strength and physical properties in sedimentary rocks: Journal of Petroleum Science and Engineering, **51**, 223–237, doi: 10.1016/j.petrol.2006.01.003.

Curtis, M. E., R. J. Ambrose, C. H. Sondergeld, and C. S. Rai, 2010, Structural characterization of gas shales on the micro- and nano-scales: Presented at Canadian Unconventional Resources & International Petroleum Conference, CUSG/SPE 137693.

Donath, F. A., 1961, Experimental study of shear failure in anisotropic rock: Bulletin of the Geological Society of America, **72**, 985–990, doi: 10.1130/0016-7606(1961)72[985:ESOSFI]2.0.CO;2.

Fjaer, E., R. M. Holt, P. Horsrud, A. M. Raaen, and R. Risnes, 1992, Petroleum related rock mechanics: Elsevier Science.

Hagin, P. N., and M. D. Zoback, 2004, Viscous deformation of unconsolidated sands — Part 1: Time-dependent deformation, frequency dispersion, and attenuation: Geophysics, **69**, 731–741, doi: 10.1190/1.1759459.

Hagin, P. N., and M. D. Zoback, 2010, Laboratory studies of the compressibility and permeability of low-rank coal samples from the Powder River Basin, Wyoming, USA: Presented at 44th US Rock Mechanics Symposium and 5th US–Canada Rock Mechanics Symposium, paper number 10-170.

Hill, R., 1963, Elastic properties of reinforced solids: Some theoretical principles: Journal of the Mechanics and Physics of Solids, **11**, 357–372, doi: 10.1016/0022-5096(63)90036-X.

Lockner, D., 1993, Room temperature creep in saturated granite: Journal of Geophysical Research, **98**, 475–487, doi: 10.1029/92JB01828.

Lockner, D. A., J. D. Byerlee, V. Kuksenko, A. Ponomarev, and A. Sidorin, 1992, Observations on quasistatic fault growth from acoustic emissions, *in* B. Evans, and T. Wong, eds, Fault mechanics and transport properties of rocks: Academic Press, International Geophysics Series, 3–32.

Loucks, R. G., R. M. Reed, S. C. Ruppel, and D. M. Jarvie, 2009, Morphology, genesis, and distribution of nanometer-scale pores in siliceous mudstones of the Mississippian Barnett shale: Journal of Sedimentary Research, **79**, 848–861, doi: 10.2110/jsr.2009.092.

Moore, D. E., and D. A. Lockner, 2004, Crystallographic controls on the frictional behavior of dry and water-saturated sheet structure minerals: Journal of Geophysical Research, **109**, B03401, doi: 10.1029/2003JB002582.

Paterson, M. S., and T. Wong, 2005, Experimental rock deformation — The brittle field, 2nd ed.: Springer-Verlag.

Rawling, G. C., P. Baud, and T. F. Wong, 2002, Dilatancy, brittle strength, and anisotropy of foliated rocks: Experimental deformation and micromechanical modeling: Journal of Geophysical Research, **107**, 2234, doi: 10.1029/2001JB000472.

Shea, W. T., and A. K. Kronenberg, 1993, Strength and anisotropy of foliated rocks with varied mica contents: Journal of Structural Geology, **15**, 1097–1121, doi: 10.1016/0191-8141(93)90158-7.

Sondergeld, C. H., R. J. Ambrose, C. S. Rai, and J. Moncrieff, 2010, Microstructural studies of gas shales: Presented at SPE Unconventional Gas Conference, SPE 131771.

Sone, H., 2012, Mechanical properties of shale gas reservoir rocks and its relation to the in-situ stress variation observed in shale gas reservoirs: Ph.D. thesis, Stanford University.

Sone, H., and M. D. Zoback, 2013, Mechanical properties of shale gas reservoir rocks — Part 1: Static and dynamic elastic properties and anisotropy: Geophysics, **78**, this issue, doi: 10.1190/geo2013-0050.1.

Tembe, S., D. A. Lockner, and T. Wong, 2010, Effect of clay content and mineralogy on frictional sliding behavior of simulated gouges: Binary and ternary mixtures of quartz, illite, and montmorillonite: Journal of Geophysical Research, **115**, B03416, doi: 10.1029/2009JB006383.

Townend, J., and M. D. Zoback, 2001, Implications of earthquake focal mechanisms for the frictional strength of the San Andreas fault system: Geological Society, London, Special Publications, **186**, 13–21, doi: 10.1144/GSL.SP.2001.186.01.02.

Yang, Y., and M. D. Zoback, 2011, The effects of gas adsorption on swelling, visco-plastic creep and permeability of sub-bituminous coal: Presented at 45th US Rock Mechanics Symposium, paper number 11–433.